PROCEEDINGS A

royalsocietypublishing.org/journal/rspa

Research

**Cite this article:** James KA, Kelley PL, Kang Z, Bhattacharyya A, Alacoque LR. 2023 Computational synthesis of wheeled vehicles via multi- layer topology optimization. *Proc. R. Soc. A* **479**: 20230221.
https://doi.org/10.1098/rspa.2023.0221

Received: 30 March 2023
Accepted: 4 August 2023

**Subject Areas:**
mechanical engineering, computational mechanics, computer-aided design

**Keywords:**
topology optimization, multi-body mechanisms, computational design synthesis

**Author for correspondence:**
Kai A. James
e-mail: kai.james@gatech.edu



# Computational synthesis of wheeled vehicles via multi-layer topology optimization

Kai A. James[1], Patrick L. Kelley[2], Ziliang Kang[3], Anurag Bhattacharyya[4] and Lee R. Alacoque[2]

[1]Georgia Institute of Technology, Atlanta, GA, USA
[2]University of Illinois at Urbana-Champaign, Urbana, IL, USA
[3]Massachusetts Institute of Technology, Cambridge, MA, USA
[4]Palo Alto Research Center, Palo Alto, CA, USA

KAJ, 0000-0003-2593-9762; ZK, 0000-0002-7010-6308; LRA, 0000-0001-5290-2928

In current engineering practice, computer-aided design (CAD) tools play a key role in the design and fabrication of most mechanical systems, including the design of most vehicles. This software tends to rely heavily on human designers to provide the basic design concept, with the software being used to computationally render an existing design, or to perform modifications to a design to achieve incremental improvements in performance. However, an emerging class of computational methods, known as *topology optimization* methods, offers the potential for true *black box* computational design. Under this general framework, practitioners provide the algorithm with the constitutive properties of the design materials, and the mechanical function being designed for (e.g. maximum stiffness under a given loading condition), and the algorithm autonomously generates a description of the corresponding structure. With some exceptions, existing topology optimization methods are limited to generating static, single-body designs. In this study, we present a novel method that builds upon the current state of the art by combining multiple collocated planar design domains to achieve automated computational synthesis of multi-body wheeled vehicles. This capability represents an important step on the path toward automated computational design of increasingly complex, innovative and impactful mechanical systems.



THE ROYAL SOCIETY PUBLISHING

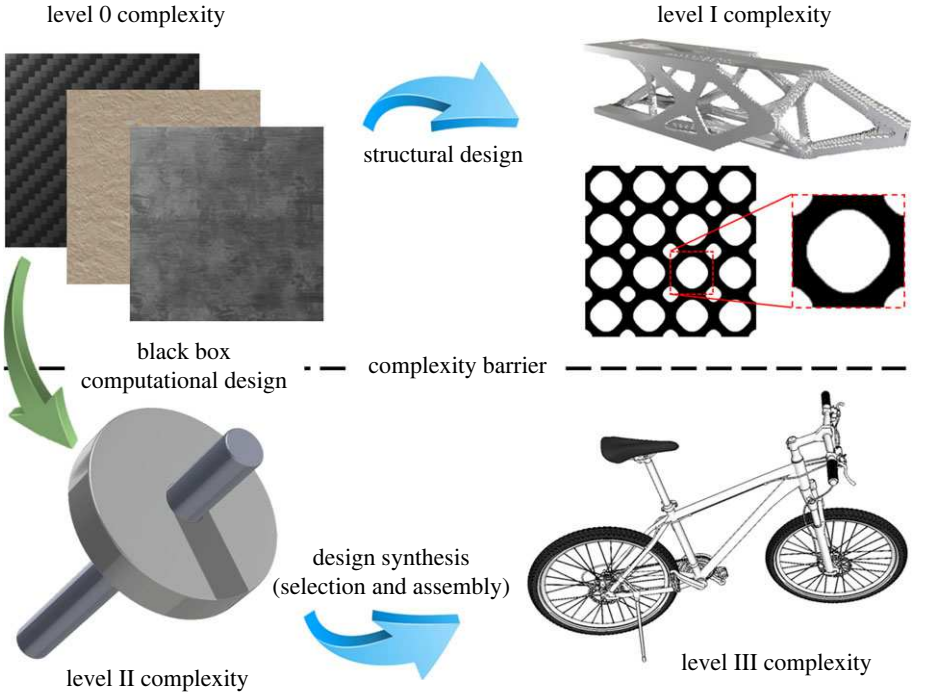


**Figure 1.** The four levels of mechanical complexity. Current structural design algorithms take Level 0 complexity information as input and generate Level I complexity structures. Our algorithm makes the leap to Level II, given only Level 0 information.

# 1. Introduction

## (a) Background

Wheeled transport mechanisms represent a crucial frontier in mechanical design. At its core, engineering design can be understood as a process of creating purposeful complexity. Design algorithms receive input information that describes the physics and behaviour of the design materials or design components, and they use the input to generate a more complex system with a specific engineering function. In the context of purely mechanical systems (i.e. those not reliant on electrical or chemical processes), there exist four broad levels of complexity: the lowest level includes raw materials in their natural form, having no organization or structure beyond their natural heterogeneity and molecular composition. Hereafter, we refer to this class of systems as having *Level 0* complexity. The next stage of complexity (*Level I*) includes single-body structures and architected materials. Level I systems are largely static, with all motion caused by elastic and inelastic material deformations or *strains*. Systems with *Level II* complexity contain two or three moving parts that are combined to perform a basic mechanical function. This class of systems includes compound machines like a wheelbarrow or a pair of pliers. Lastly, we have Level III complexity, which refers to complex machines containing chains of many (often 10 or more) Level I and Level II components (figure 1). This class of systems includes bicycles and mechanical clocks (table 1).

Current mechanical design algorithms generally fall within one of two categories. In one camp, we have structural design algorithms, which receive Level 0 input and generate Level I designs. These algorithms typically use gradient-based optimization to tailor the size, shape and topology [1] of the structural features to produce highly specialized structures [2,3], mechanisms [4,5] and materials [6]. In the other camp, we have algorithms that receive Level II information describing

**Table 1.** Nomenclature.

| | |
|---|---|
| $A_T$ | maximum elevation of terrain |
| $a, b$ | arbitrary constants |
| $\boldsymbol{a}$ | axle location |
| $a_y$ | $y$-coordinate of axle location |
| $C_{\max}$ | maximum allowable compliance |
| $\mathbf{F}$ | global vector of applied forces |
| $g$ | acceleration due to gravity |
| $g_1, g_2$ | constraint functions |
| $\Delta h$ | change in height of axle |
| $\mathbf{K}$ | global stiffness matrix |
| $\mathbf{K}_B$ | contribution of barrow layer to global stiffness matrix |
| $\mathbf{K}_W$ | contribution of wheel layer to global stiffness matrix |
| $\mathbf{K}_C$ | contribution of contact springs to global stiffness matrix |
| $\mathbf{k}$ | effective stiffness matrix of element |
| $\mathbf{k}_0$ | nominal stiffness matrix of element |
| $\mathbf{k}_c$ | contact stiffness matrix |
| $\mathbf{k}'$ | rotated stiffness matrix |
| $m$ | total mass of the axle, carriage and cargo |
| $n_e$ | number of elements |
| $n_s$ | number of spokes |
| $n_v$ | number of wheel vertices |
| $P$ | perimeter of wheel |
| $P_{\min}$ | minimum allowable perimeter of wheel |
| $\boldsymbol{p}$ | contact point of wheel on terrain |
| $p_y$ | $y$-coordinate of contact point |
| $p$ | stiffness penalization constant |
| $\mathbf{R}$ | rotation matrix |
| $R$ | spoke length |
| $\boldsymbol{r}$ | line segment joining the ends of two neighbouring spokes |
| $s$ | arc length of terrain |
| $T$ | terrain height |
| $\mathbf{U}$ | global vector of nodal displacements |
| $V_{\max}$ | maximum allowable material volume |
| $W$ | total work |
| $X$ | horizontal spatial coordinate |
| $\boldsymbol{x}$ | set of optimal spoke lengths |

(*Continued.*)

**Table 1.** (*Continued.*)

| | |
|---|---|
| $x_n$ | nodal $x$ coordinate |
| $\gamma$ | vertical spatial coordinate |
| $y_n$ | nodal $y$-coordinate |
| $\boldsymbol{\alpha}$ | set of optimal spoke orientation angles |
| $\beta$ | angle from the horizontal to the line segment $\boldsymbol{r}$ after the rotation |
| $\gamma$ | angle from the horizontal to the line segment $\boldsymbol{r}$ before the rotation |
| $\zeta_x^*, \zeta_y^*$ | contact point within the design domain |
| $\theta$ | rotation angle |
| $\kappa_0$ | nominal contact stiffness |
| $\lambda_T$ | terrain wavelength |
| $\rho$ | element relative material density |
| $\sigma$ | steepness of contact stiffness decay |

a set of rudimentary building blocks. The algorithm then synthesizes complex kinematic chains (Level III) by systematically selecting and assembling the various components [7–9]. Figure 1 contains an illustration of the complexity categories and the role of the various algorithms in producing purposeful complexity. Existing algorithms are very efficient at solving these two distinct design problems. However, we currently lack effective means of automatically making the leap from Level 0 to Level II complexity. Traversing this barrier represents a significant advancement in design automation. For this reason, we seek to create an algorithm that can autonomously synthesize a wheeled vehicle (Level II complexity) using a series of level 0 building blocks. The algorithm is given only the mechanical properties of the design material, the boundary conditions of the black box domain within which the design must be created, and a mathematical description of the desired mechanical function.

This approach to computational design in which the design domain is treated as a black box has its roots in *topology optimization* [10,11]. This term refers to a class of methods in which the algorithm generates an optimal structure by systematically distributing material within the design domain to create a design that performs optimally with respect to a given objective (figure 2). Topology optimization algorithms are typically used to generate level I systems (i.e. single-bodied static structures and metamaterials) [12,13]. Several authors have noted that the designs obtained through topology optimization appear organic in their material pattern, and their appearance has been compared to the microstructure of human bone tissue [14] and bird beaks [15].

## (b) Formulation of the design problem

We focus our investigation on a wheelbarrow-style vehicle. The wheelbarrow has two primary components: the wheel and the 'barrow', which typically includes a container, a set of handles and an axle. All parts that comprise the 'barrow' are fixed with respect to one another; therefore, conceptually they can be treated as a single component. We solve the resulting two-body design problem using numerical optimization whereby we mathematically represent the design as a set of parameters which contain a full description of the design's geometry, connectivity and material distribution. We then define an objective function, which provides a quantitative measure of how well each design performs. Optimization algorithms search the space of potential designs (i.e. all possible combinations of all design parameter values) to find the precise set of values which cause the objective function to be minimized, and this combination will correspond to the optimal design for the prescribed performance objective. Using this general strategy, the algorithm must

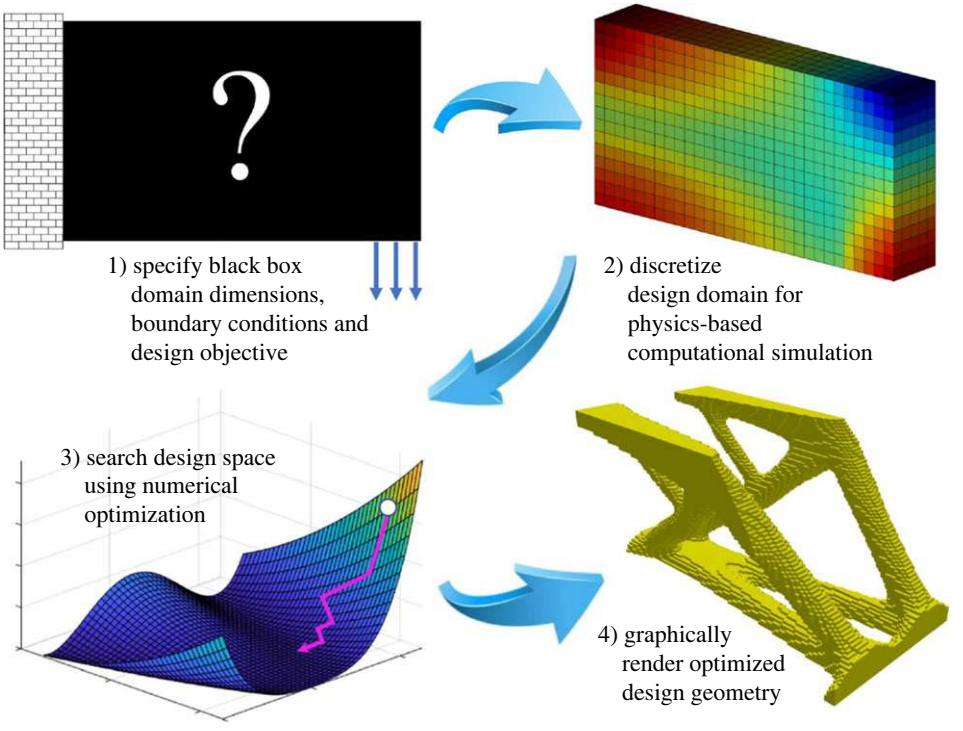


**Figure 2.** Black box design using topology optimization.

deduce the optimal structure for the barrow, and the optimal shape, size, location (relative to the fixed axle) and spoke configuration of the wheel. This problem is particularly challenging because we must model contact along a design-dependent surface (i.e. the circumference of the wheel), and we must simultaneously optimize the structure of two distinct but inter-connected elastic bodies, all while maintaining the continuity and smoothness of the optimization problem.

The objective of our design problem is to minimize energy expenditure. We seek a design for our wheelbarrow that requires the operator to use as little energy as possible in transporting cargo from point A to point B. In our energy model, we assume a frictionless axle. This assumption is consistent with the fact that, when bearings are used, frictional losses are negligible, with most rolling resistance caused by hysteresis due to inelastic deformations within the wheel system [16]. The second assumption is that the rolling motion is slow and quasi-static; therefore, there is no kinetic energy or *coasting*. We also assume a rigid rolling surface and pure rolling with no slippage at the wheel–ground interface. With these assumptions in place, we can express the total energy expenditure as a function of the wheel shape. We then instruct the design algorithm to search for the optimal wheel shape and internal structural layout that yields the most energy-efficient performance. Using this method, we can optimize for rolling over both flat and curved periodic surfaces. The optimal wheel shape is that which causes the axle (and the cargo it supports) to traverse a straight, level path throughout the rolling motion. Figure 3 illustrates the rolling motion of a wheel whose shape has been optimized for sinusoidal terrain.

## (c) Literature survey

Topology optimization has been successfully applied to the design of a variety of structures ranging from aircraft wings [15,17–19] to biomedical devices [20,21]. Several studies have also applied topology optimization to the design of wheel structures [22,23]; however, in all of these studies the wheel shape was given to the algorithm as input, and topology optimization was

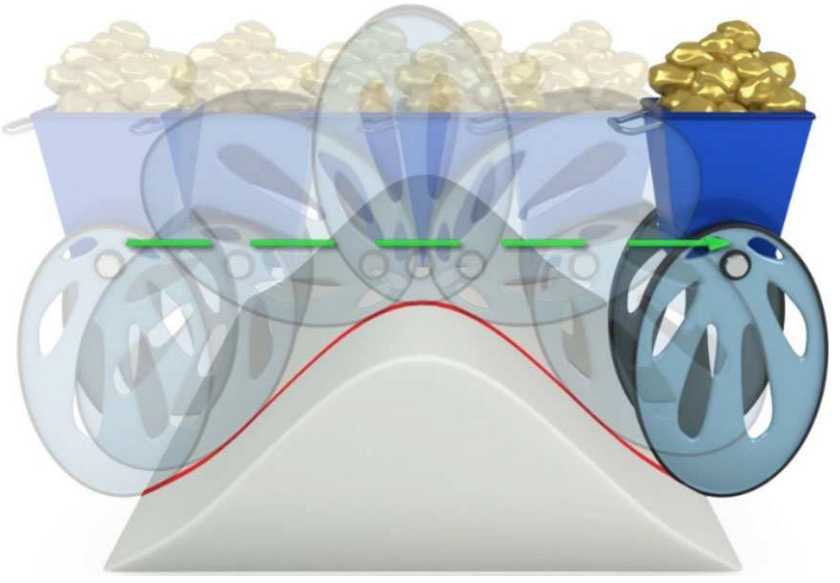

**Figure 3.** Motion of a shape-optimized wheelbarrow rolling over sinusoidal terrain, with the trajectory of the axle represented by the green dashed line. Because the wheel is optimized for the terrain topography, the axle and cargo remain at a constant height throughout the motion, thus minimizing energy expenditure.

used to create the stiffest possible structure within this prescribed shape. The current study differs from its predecessors in that we assume nothing about the wheel's shape, leaving the algorithm to deduce the optimal shape and internal structural geometry autonomously. Therefore, our proposed method combines shape and topology optimization along with a novel contact model that captures the interaction between the ground and the wheel's outer surface.

Combining shape and topology optimization into single simultaneous algorithms has been done before in various ways. Some approaches optimize topology using an explicit representation of a structure's shape [24,25]. Others simultaneously optimize the three-dimensional shape of a surface and the two-dimensional material topology within it, such as for the design of shell structures [26,27]. There are also methods where explicitly defined shapes are combined with completely free-form topology optimization, such as for shape optimization of a pre-stressing tendon embedded within a topology optimized concrete beam [28], for shape and positioning optimization of a battery pack within a structural frame [29] or for finding the optimal shapes and locations of boundary conditions in topology optimization [5]. Previous studies have also used numerical optimization methods to synthesize multi-body dynamic systems [30,31], or individual components with loading conditions based on analysis of the system [32]. Notable among these efforts is an August 2000 study authored by Lipson and Pollack in which they used a genetic algorithm (an optimization method that mimics the process of evolution by natural selection) together with additive manufacturing to autonomously synthesize and fabricate self-sustaining robots [7]. This algorithm used a series of pre-defined structural building blocks that were assembled to create robots with optimal locomotive performance.

Topology optimization has also been used to generate rigid body mechanisms. One study by Luo *et al*. [33] synthesizes mechanisms by optimizing the number, type and location of joints connecting overlapping planes. Another by Kim *et al*. uses topology optimization to design the rear suspension linkage of a vehicle using simple bar and spring elements [34], and in one study by Briot & Goldszetejn [35] the structural topology of the links in a five bar mechanism were optimized. Here the rigid body representation was defined beforehand and the link sizes were not optimized by the algorithm.

### (d) Scope and contributions of this study

All of the studies described above use iterative procedures to systematically search the design space, with the actual design gradually evolving toward a desirable solution. However, the current study is the first to attempt iterative black box design to create a multi-body wheeled vehicle. In this way, we seek to advance an emerging paradigm in computational design, where algorithms autonomously create complex systems with minimal input from human designers.

The ability of the proposed algorithm to synthesize a multi-body wheeled transport mechanism represents an important capability in computational design and design automation. The design framework presented in this study contains several key contributions. These include a unique design representation scheme that enables simultaneous shape and topology optimization, an original contact model that preserves the continuity of the design space and therefore allows for gradient-based optimization, an optimization problem formulation that frames the design task as an energy minimization problem, and a new multi-layer topology optimization formulation that accommodates 360° rigid body rotation. Together, these features enable new design capabilities that can be applied to the design and synthesis of a variety of mechanical components that rely on relative rotational motion between attached bodies. Furthermore, by providing increased autonomy and design freedom to the algorithm, this paradigm can yield improvements in system performance, as the final design depends less on human intuition, and is instead determined mathematically based on optimality criteria.

### (e) Organization of the paper

The remaining sections of the paper are organized as follows. In §2, we provide a detailed description of methodology used to implement the algorithm, including the underlying mathematical theory. In §3, we present the results of the proposed computational design process along with some discussion on the significance of these results. Lastly, §4 contains concluding remarks, including a summary of the study and directions for future work.

## 2. Methods

Shape optimization, along with sizing and topology optimization, is one of three foundational approaches to structural optimization. It is regularly used to improve both structural performance and aerodynamic performance [36], since small changes in shape can lead to significant increases in aerodynamic drag. In the current study, we represent the wheel shape parametrically by a series of $n_s$ spokes emanating from a central point that corresponds to the location of the axle within the plane of the wheel. Each spoke is allowed to rotate freely within an assigned sector or *wedge*, as shown in figure 4. For each spoke, we optimize the orientation angle as well as the spoke length, which is defined as the distance from the spoke tip to the axle location. The wheel's outer shape is given by the polygon obtained when we connect the spoke tips in a clockwise sequence. Note that the spokes are not actual structural members, but rather, they are a series of virtual line segments used to mathematically represent the wheel's shape. The shape optimization is simply a matter of finding the set of optimal spoke lengths, $\boldsymbol{x}$, and orientation angles, $\boldsymbol{\alpha}$, that correspond to the most energy-efficient wheel shape.

### (a) Terrain representation

We consider both flat and curved rolling surfaces that can be represented as periodic sinusoidal functions. Within the *xy* Cartesian plane occupied by the wheel, the terrain height is given by the following function:

$$T(X) = \frac{A_T}{2}\left[1 - \cos\left(\frac{2\pi}{\lambda_T}X\right)\right], \tag{2.1}$$

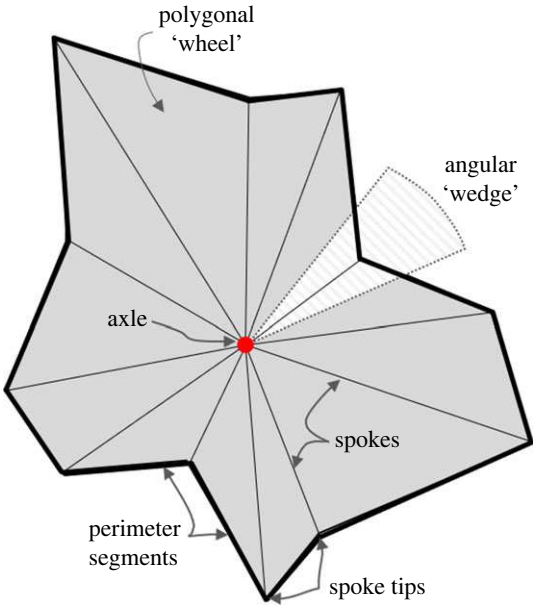


**Figure 4.** Polygonal wheel representation containing spokes and wedges.

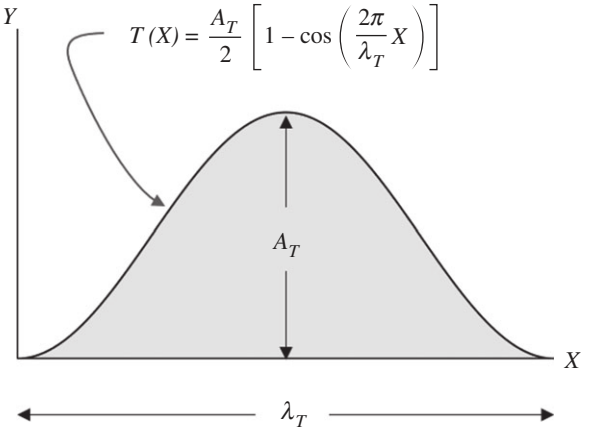


**Figure 5.** Illustration of the sinusoidal terrain profile.

where $A_T$ is the maximum elevation (i.e. amplitude) and $\lambda_T$ is the terrain's wavelength, and $X$ is the position along the horizontal axis. Figure 5 contains an illustration of the resulting curve in the $xy$-plane. In all cases, we assume that gravity is aligned with the $y$-axis.

Note that in the example problem presented above, we have chosen a sinusoidal terrain profile because the optimal wheel shape for this terrain has a closed-form analytical solution (i.e. the elliptical wheel). Therefore, we can validate the output of our numerical shape optimization method by comparing it against the known analytical solution. The proposed method requires that the terrain is continuous, periodic, and can be represented as a function $Y(X)$ with one-to-one mapping from $X$ to $Y$.

## (b) Simulation and evaluation of the work function

The goal of the optimization procedure is to find the wheel shape that causes the operator to expend minimal energy per unit distance travelled. Therefore, we minimize the total energy expenditure (i.e. mechanical *work*) associated with a single revolution of the wheel, while

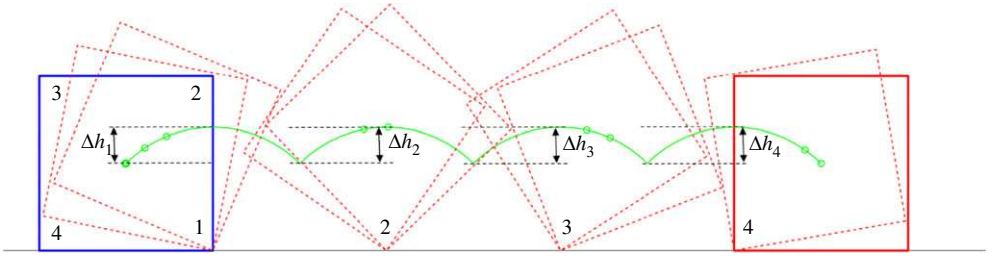


**Figure 6.** Motion of a suboptimal wheel rolling over flat terrain, with the axle trajectory shown in green, and vertices numbered according to the order of contact with the ground.

enforcing a lower bound on the total wheel circumference, which is equivalent to the distance travelled during a single revolution. The total work is directly proportional to the cumulative increase in the height of the axle during the rolling motion. For a suboptimal wheel shape, this quantity will be non-zero as shown in figure 6, where we trace the path of the axle within a square wheel rolling over a flat surface. For the four-sided polygonal wheel, there are four peaks in the axle trajectory, one for each vertex in the wheel shape. For each peak, we can compute $\Delta h$, which is the increase in the height of the axle. For a frictionless axle, the total work is equal to the total gravitational potential energy associated with lifting the axle (along with the cargo that it supports) through a distance of $\Delta h$. Therefore, the total work, $W$, is given by

$$W = mg \sum_{i=1}^{n_v} \Delta h_i, \tag{2.2}$$

where $m$ is the total mass of the axle-carriage component plus the cargo contained within the carriage, $g$ is the acceleration due to gravity, and $n_v$ is the number of wheel vertices. Note that we have assumed slow, quasi-static motion, therefore the wheel is not allowed to coast during the descent portions of the axle trajectory, and there is no kinetic energy available to offset the required energy expenditure of the operator. This assumption corresponds to the hypothetical scenario in which the wheelbarrow is being used to transport delicate cargo. We evaluate the work function by simulating the rolling motion. A complete revolution can be broken down into a sequence of pivots about the point where a given wheel vertex makes contact with the ground, as shown in figure 7. The figure depicts the rotation of the wheel about the tip of spoke $i$ in the $xy$-plane. During this particular rotation increment, the triangle formed by spoke $i$ and spoke $i+1$ pivots until the tip of spoke $i+1$ makes contact with the ground. During each rotation increment, $i$, we implement the following four-step procedure to compute the amount of work required for each rotation increment.

1. Compute the $xy$ coordinate of the next contact point, $p^{i+1}$, using an iterative Newton–Raphson procedure, where $p^{i+1}$ is given by the intersection of the terrain, $T(X)$, and the rotating line segment, $r_i$, which connects the tips of spoke $i$ and spoke $i+1$.
2. Compute the rotation angle $\theta^i$ using $\theta = \gamma - \beta$, where $\gamma$ and $\beta$ are the angles from the horizontal to the line segment $r_i$ before and after the rotation.
3. Compute the $xy$-coordinates of the new axle location $a^i$.
4. Evaluate the peak change in the axle height during the rotation, $\Delta h_i$.

Note that in step 4 of the above procedure, we must account for three mutually exclusive cases: in case I, the axle rises monotonically throughout the duration of the rotation increment, in which case we have

$$\Delta h_i = a_y^{i+1} - a_y^i, \tag{2.3}$$

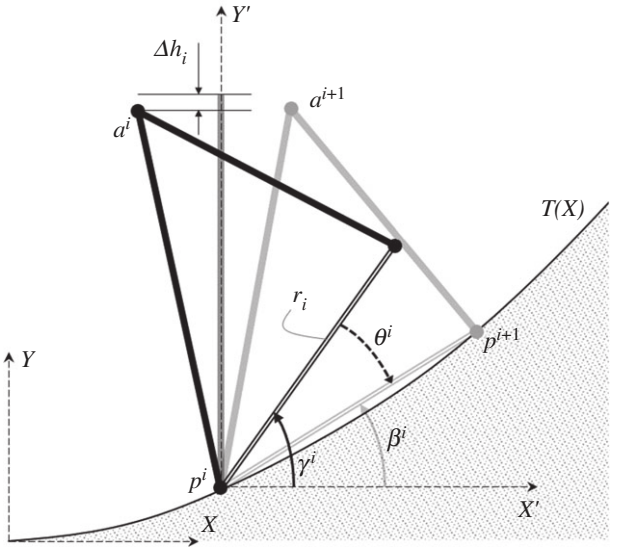


**Figure 7.** Schematic depicting a single rotation increment during the rolling process, with the black triangle representing a sector within a polygonal wheel. Here, *a* represents the axle location, *p* represents the *pivot* point at which the spoke tip makes contact with the terrain, $T(X)$, and $\Delta h_i$ represents the peak change in axle height during the rotation.

where $a_y^{i+1}$ is the $y$-coordinate of the axle location when the tips of spoke $i$ and spoke $i+1$ are in contact with the terrain. In case II, the axle rises only during the initial portion of the rotation. It reaches a peak height when spoke $i$ is in a vertical position, and then the axle descends until contact is made at point $p^{i+1}$ (figure 7). In this case, the peak change in the axle height is given by

$$\Delta h_i = p_y^i + R_i - a_y^i, \tag{2.4}$$

where $R_i$ is the length of spoke $i$. In case III, the axle descends monotonically during the entire rotation increment. In this case, $\Delta h_i = 0$.

Because the suboptimal wheel is generally non-convex (prior to the completion of the optimization procedure), it is possible that the position in which spoke $i+1$ touches the ground may cause subsequent spokes to penetrate the terrain. This corresponds to a non-physical scenario; however, this does not affect the execution of the algorithm. The equations presented above are applicable whether the wheel is rolling forward or backward. Therefore, we allow spokes to penetrate the terrain during the simulation, and if the tip of spoke $i+1$ is below the terrain surface at the beginning of rotation increment $i$, then the wheel must rotate backward until the tip reaches the terrain's surface. Any subsequent increase in height that follows the backward rotation is included in the total work computation. Therefore, during the optimization search, the algorithm naturally penalizes non-convex wheel geometries that cause penetration.

## (c) Perimeter constraints

For the case of flat terrain, we enforce a lower bound on the total perimeter, since a small wheel circumference will require less work per revolution. This is due to the fact that we approximate the circumference of the wheel as a piecewise linear polygon. For a smooth circular wheel, the total work expenditure due to gravitational losses will be zero regardless of wheel size. By enforcing this perimeter constraint while minimizing the energy expenditure for one revolution, we effectively minimize the work per unit distance travelled. In the case of sinusoidal terrain, we constrain the total perimeter of the wheel to match the arc length of a single period within

the wave pattern. This ensures that the total energy expenditure is minimized across multiple revolutions of the wheel. We compute the arc length of the terrain, $s$, over one wavelength, $\lambda_T$, using the integral given in equation (2.5).

$$s = 2\int_0^{\lambda_T/2} \sqrt{1 + \left(\frac{dT}{dX}\right)^2}\, dX, \tag{2.5}$$

where $T$ is the terrain elevation as defined in equation (2.1). Evaluating the perimeter of the wheel, $P$, is simply a matter of summing the lengths of all line segments, $r_i$, that connect adjacent spoke tips.

## (d) Optimization problem formulation

Once we are able to evaluate the work function, the perimeter function and the arc length of the terrain, we define the numerical optimization problem as follows:

$$\left.\begin{aligned} &\min_{\boldsymbol{x},\boldsymbol{\alpha}} && W(\boldsymbol{x},\boldsymbol{\alpha}) \\ &\text{subject to:} && g_1(\boldsymbol{x},\boldsymbol{\alpha}) = s - P(\boldsymbol{x},\boldsymbol{\alpha}) \le 0 \\ &&& g_2(\boldsymbol{x},\boldsymbol{\alpha}) = P(\boldsymbol{x},\boldsymbol{\alpha}) - s \le 0. \end{aligned}\right\} \tag{2.6}$$

Note that in the case of the flat terrain, we only enforce the constraint $g_1$, which ensures that $P$ is greater than the prescribed lower bound, $s$, in the final design. When enforced together, the two constraints $g_1$ and $g_2$ are mathematically equivalent to an equality constraint in which $P = s$, thus ensuring that the wheel traverses exactly one wavelength with each revolution. The above optimization problem is solved numerically using the *method of moving asymptotes*, a gradient-based optimizer [37]. All gradients (i.e. design sensitivities) are computed analytically by direct differentiation of the work and perimeter functions.

### (i) The topology optimization procedure

Topology optimization is a mathematical method for obtaining optimal geometries and configurations for the design of structures. The design task is framed as a material distribution problem in which the algorithm must determine the optimal layout of material within a prescribed design domain for a given set of loads and boundary conditions. The design domain is initially discretized into a grid of *finite elements*, and the optimization algorithm must determine which elements should be *solid* (i.e. containing material), and which elements should be *void* in the optimal structure. The output of the algorithm is a pixelized or voxelized element-by-element representation of the optimal structure as shown in figure 2.

We model the elastic deflection of the structural domain using finite-element analysis. From the displacement field, we are then able to compute more meaningful quantities like tip deflection, maximum stress and structural compliance. Using the discretized finite-element mesh, the global vector of nodal displacements, $\mathbf{U}$, is computed using equation (2.7)

$$\mathbf{KU} = \mathbf{F} \Rightarrow \mathbf{U} = \mathbf{K}^{-1}\mathbf{F}, \tag{2.7}$$

where $\mathbf{F}$ is the global vector of applied forces and $\mathbf{K}$ is the global stiffness matrix. This governing equilibrium equation is obtained from a discretization of the Navier–Lamé equations with prescribed Dirichlet and Neumann boundary conditions. It assumes linear elasticity with small strains. The global stiffness matrix is obtained by assembling the element stiffness matrices such that

$$\mathbf{K} = \tilde{\sum_i}\, \mathbf{k}_i. \tag{2.8}$$

Here the summation operator, $\tilde{\Sigma}$, denotes matrix assembly in which we sum the individual stiffness contributions of all elements by adding them to the appropriate rows and columns of $\mathbf{K}$

according to their inter-element connectivity. The effective stiffness matrix, $\mathbf{k}_i$, of each element is determined by an interpolation function as shown below.

$$\mathbf{k}_i = \rho^p \mathbf{k}_0. \tag{2.9}$$

Here $\mathbf{k}_0$ is the nominal stiffness matrix corresponding to a solid element, $\rho$ symbolizes the element's relative material density, and $p$ denotes the penalization constant. Note that a material density of $\rho = 1$ corresponds to a fully solid element, while a material density of $\rho = 0$ indicates a void element. The material densities serve as the design parameters in the optimization problem, and together they provide a complete description of the structural topology. This particular interpolation strategy is known as the *Solid Isotropic Material with Penalization* (SIMP) formulation [38]. It allows elements to assume hybrid states along the solid-void continuum, which is necessary for efficient gradient-based optimization. However, when $p > 1$, the formulation effectively penalizes intermediate density states with a reduced stiffness-to-weight ratio, thus incentivizing the optimizer to select designs containing only fully solid or fully void elements. When successful, the algorithm will converge to a binary design that can be easily interpreted and fabricated via additive manufacturing.

The SIMP method is one of many methods used to mathematically represent the material distribution within a topology optimization framework. It builds upon the original homogenization-based design representation introduced by Bendsøe & Kikuchi [11]. The SIMP method was introduced shortly thereafter, and soon came to dominate the topology optimization landscape due to its conceptual simplicity and high degree of versatility, which allows it to be deployed in the design of a wide range of structures governed by a variety of physics models, from concrete structures subject to brittle damage [39] to aircraft structures subject to aerodynamic loading and fluid–structure interaction [16].

Since the introduction of the SIMP method, researchers have developed other strategies for solving the material distribution problem. These methods include the level set method [40], sequential element rejection and admission (SERA) [41], evolutionary algorithms including genetic algorithms [42], generative adversarial networks (GANS) [43] and geometry projection [44]. Each of these approaches offers unique advantages and disadvantages. For example, the level set method yields a sharp, well-defined material interface; however, the optimization search can also be sensitive to the initial guess, and extra steps must be taken to allow the algorithm to nucleate new holes in two-dimensional problems [45]. Gradient-free methods like genetic algorithms are known to be highly computationally expensive and may be impractical for high-dimensional problems [46]. Similarly, data-driven methods like GANS require thousands of training examples, which must be generated using traditional gradient-based methods [43]. This makes the total cost of the method highly computationally expensive.

Like the methods described above, the SIMP method has its disadvantages. Specifically, the optimized designs can be mesh-dependent [47] and they can contain fuzzy boundaries at the material interface [48]. In the current study, we resolve these issues using density filtering [49], and Heaviside projection [48], with little additional computational cost. Additionally, the topology optimization problems solved in this study are non-convex. Consequently, the proposed problem formulation is subject to local minima, and therefore it is possible to converge to different designs if one were to change the initial values of the design parameters. This issue is present in all topology optimization methods [46,47], including those mentioned above. It can be mitigated by choosing an appropriate initial material distribution. Here we begin all topology optimizations with a fully solid design domain in which all elements have full material density. Research has indicated that local minima occur at binary locations within the design space (i.e. designs containing both solid and void regions in which all elements have either fully solid or fully void density [50]). Hence, by starting with a uniform material distribution, we are able to avoid convergence to in inferior local minimum.

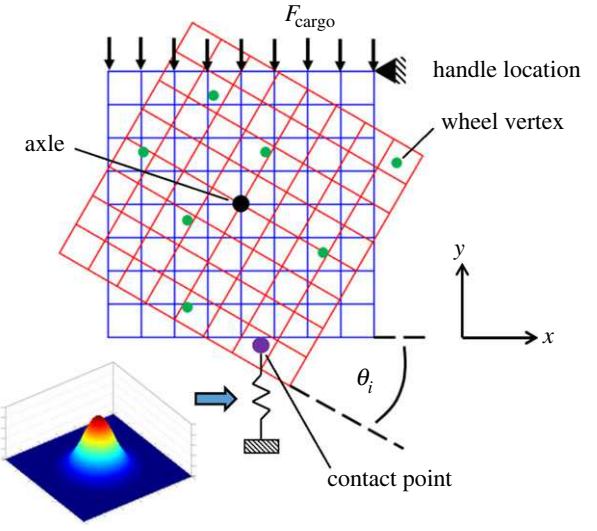


**Figure 8.** Domain and boundary conditions for the multi-body wheelbarrow design problem, with the wheel layer shown in red and the barrow layer shown in blue. The algorithm identifies the lowest vertex in the wheel layer and activates a contact boundary condition at that location to simulate contact with the ground.

## (e) Multi-body design

The multi-body design problem involves simultaneously optimizing the shape and topology of multiple inter-connected elastic bodies. To perform this task, we use a multi-layer topology optimization framework in which we define multiple two-dimensional design domains that are collocated within the $xy$-plane [51]. Each domain comprises a *layer* that will evolve into an optimized component during the design process. We perform concurrent topology optimization of all layers by computing the global elastic response of the combined multi-body system. The layers are connected via pin joints, which restrict relative translational motion, but allow connected bodies to undergo rigid body rotation with respect to one another. For the wheelbarrow design problem, the axle is modelled as a pin joint.

In the current problem formulation, we include one layer each for the wheel and barrow components. We then apply appropriate boundary conditions to each layer according to the desired functionality (figure 8). To simulate the loading caused by the rolling of the wheel we discretize the rolling motion into a series of evenly spaced rotation increments. Each increment is characterized by the angle, $\theta_i$, that the wheel layer forms with the $x$-axis at the end of the rotation increment.

## (f) The contact model

There have been several previous efforts for contact modelling in topology optimization, for example, modelling sliding contact between two-component structure interfaces [52], contact of elastic bodies against rigid obstacles [53], contact between multiple interlocking components [54], and internal contact modeling for large-strain structures [55]. Here we seek to model a dynamic rotating component in contact with another rigid surface, and therefore have developed our own contact model specifically for this kind of problem.

For each rotation increment, given the corresponding orientation of the wheel layer, the algorithm computes the rotated position of all vertices using rotation matrices. The algorithm then identifies which wheel vertex is in contact with the ground by finding the vertex with the lowest $y$-coordinate expressed in the global reference frame. We then insert a virtual spring, connecting

the *contact* vertex to a fixed support, as shown in figure 8. The contact spring provides stiffness in both the $x$- and $y$-directions. This is designed to capture the effect of a static friction force exerted by the ground on the wheel. In this way, we mimic the effect of the polygonal wheel pivoting about the fixed contact point with the ground during the rotation increment. The outcome is a numerical simulation of a no-slip rolling condition.

If the stiffness of the contact spring is infinite, this corresponds to a rigid ground. However, for practical and numerical purposes we keep the spring stiffness finite, which maintains continuity and smoothness of the optimization problem. Furthermore, rather than treating the contact location as an infinitesimal point in the $xy$-plane, we model the contact point as a finite region whose stiffness follows a Gaussian distribution as shown in figure 8. The peak of the distribution function is located at the actual contact point $(\zeta_x^*, \zeta_y^*)$ and the contact stiffness exhibits a Gaussian decay as one moves further from the contact point. Within the finite-element model, we add a contact stiffness, $\mathbf{k}_c$, to all nodes in the wheel's finite-element mesh, with each node's contact stiffness computed according to its distance from the current contact point. Therefore, for a node located at a point $(x_n, y_n)$, that node's contact stiffness is computed as

$$\mathbf{k}_c = \begin{bmatrix} 1 & 0 \\ 0 & 1 \end{bmatrix} \kappa_0 \sigma \sqrt{2\pi} \exp\left( - \left[ \frac{(\zeta_x^* - x_n)^2 + (\zeta_y^* - y_n)^2}{2\sigma^2} \right] \right), \tag{2.10}$$

where $\sigma$ is a constant used to control the steepness of the decay in the stiffness distribution, and $\kappa_0$ is the nominal stiffness of the pin joint used to simulate contact.

## (g) Multi-body structural analysis

To account for the changing orientation of the wheel layer with respect to the rotationally fixed barrow layer, we apply a rotation operation to the stiffness matrices of the elements in the wheel mesh. For a given element with stiffness matrix $\mathbf{k}$ and orientation angle $\theta$ the rotated stiffness matrix, $\mathbf{k}'$, is given by

$$\mathbf{k}' = \mathbf{R}(\theta_i)\mathbf{k}\mathbf{R}(\theta_i)^T, \tag{2.11}$$

where the rotation matrix $\mathbf{R}$ is computed as

$$\mathbf{R}(\theta_i) = \begin{bmatrix} \boldsymbol{R}_W & 0 & 0 & 0 \\ 0 & \boldsymbol{R}_W & 0 & 0 \\ 0 & 0 & \boldsymbol{R}_W & 0 \\ 0 & 0 & 0 & \boldsymbol{R}_W \end{bmatrix}, \boldsymbol{R}_W(\theta) = \begin{bmatrix} \cos(\theta) & -\sin(\theta) \\ \sin(\theta) & \cos(\theta) \end{bmatrix}. \tag{2.12}$$

During each rotation increment, $i$, we compute the global stiffness matrix, $\mathbf{K}$, as the sum of the stiffness contributions from the barrow layer $\mathbf{K}_B$, the wheel layer $\mathbf{K}_W$, and the contact springs $\mathbf{K}_C$, so that

$$\mathbf{K} = \begin{bmatrix} \mathbf{K}_B & 0 \\ 0 & \mathbf{K}_W + \mathbf{K}_C \end{bmatrix}, \tag{2.13}$$

where $\mathbf{K}_C$ is a global assembly of the contact stiffnesses associated with all nodes in the wheel mesh. When solving for the nodal displacements, $\mathbf{U} = \mathbf{K}^{-1}\mathbf{F}$, we treat the axle location as a shared node at which the two layers have identical displacement. Note that the contact stiffness model can also be used to model inter-layer pin joints. In this way, we could also optimize the axle location; however, in the examples presented, the axle location is fixed within the two layers. Because the optimizer is free to move the wheel relative to the axle, optimizing the axle location would be redundant. Note also that this method results in a linear algebraic system, which we use to solve for the displacement state during each rotation increment. This is in contrast to previous methods for optimizing multi-part mechanisms, in which the algorithm performs nonlinear analysis of flexible multi-body systems [51,56]. With this linear model, the numerical accuracy is determined by the accuracy of the solution of the linear system, which we solve using a direct method. Therefore, with modest computational effort, we obtain accurate displacement fields,

which we can use to compute the design sensitivities. This also ensures reliable convergence of the optimization method.

The optimization problem statement for the multi-body structural topology design problem is given in equation (2.14). We minimize the weight of the combined wheelbarrow system, while constraining the structural compliance during each load increment. Here, the compliance is proportional to the total elastic strain energy within the structure, and by constraining this quantity, we enforce a lower bound on the structural stiffness [57].

The numerical optimization problem is solved using the method of moving asymptotes, the source code for which is available for academic use. We compute all constraint function derivatives using the adjoint method, a full description of which can be found in [51].

$$\left.\begin{aligned} &\min_{\boldsymbol{\rho}} \sum_{j=1}^{n_e} \rho_j \\ &\text{subject to:} \mathbf{F}^T\mathbf{U}_i - C_{\max} \leq 0; \quad \text{for } i = 1, 2, \ldots, n_s. \end{aligned}\right\} \tag{2.14}$$

Note that the maximum allowable compliance, $C_{\max}$, must be chosen based on the maximum expected vertical deflection of the wheelbarrow along the surface to which the cargo load is applied. Based on this deflection, the size of the wheelbarrow, and the mass density of the intended cargo, we can compute the corresponding maximum compliance.

## (h) Simultaneous shape and topology design

To simultaneously design the wheel shape and the structural topology of the wheelbarrow system, we simply combine the shape and topology optimization formulations described above. The Gaussian-based distributed contact model described in equation (2.10) enables us to continuously map discrete contact points onto the finite-element mesh, while maintaining smoothness within the design space. This is essential for solving the combined shape and topology design problem in which the location of the contact point within the wheel is subject to design, and therefore must be treated as a design variable. Note that there is one-way coupling between the shape and topology design modules, as the structural loads depend on the location of the wheel vertices. We account for this coupling when minimizing the work function with respect to the spoke lengths ($\boldsymbol{x}$), the spoke angles ($\boldsymbol{\alpha}$), and the element densities ($\boldsymbol{\rho}$). This minimization is subject to constraints on the structural compliance ($C$) caused by each load case (i.e. rotation increment), the total structural volume ($V$) of both the wheel and barrow components, and the perimeter ($P$) of the wheel. The resulting coupled shape and topology optimization problem statement is given below.

$$\left.\begin{aligned} \min_{\boldsymbol{x},\boldsymbol{\alpha},\boldsymbol{\rho}} \quad & W(\boldsymbol{x}, \boldsymbol{\alpha}, \boldsymbol{\rho}) \\ \text{subject to:} \quad & \mathbf{F}^T\mathbf{U}_i - C_{\max} \leq 0 \\ & \sum_{j=1}^{n_e} \rho_j - V_{\max} \leq 0 \\ & P_{\min} - P(\boldsymbol{x}) \leq 0 \end{aligned}\right\}, \tag{2.15}$$

where $V_{\max}$ is the maximum allowable volume of material and $P_{\min}$ is the minimum allowable wheel perimeter. The structural (i.e. topology) design sensitivities are computed analytically using the adjoint method, and the numerical optimization problem is solved iteratively using the method of moving asymptotes.

# 3. Results

## (a) Shape optimization

Figure 9 shows the evolution of a wheel designed for rolling over a sinusoidal terrain. The red dot indicates the location of the axle, and the dashed blue line represents the analytical solution of the shape optimization problem (i.e. the theoretical optimum). The optimizer controls the

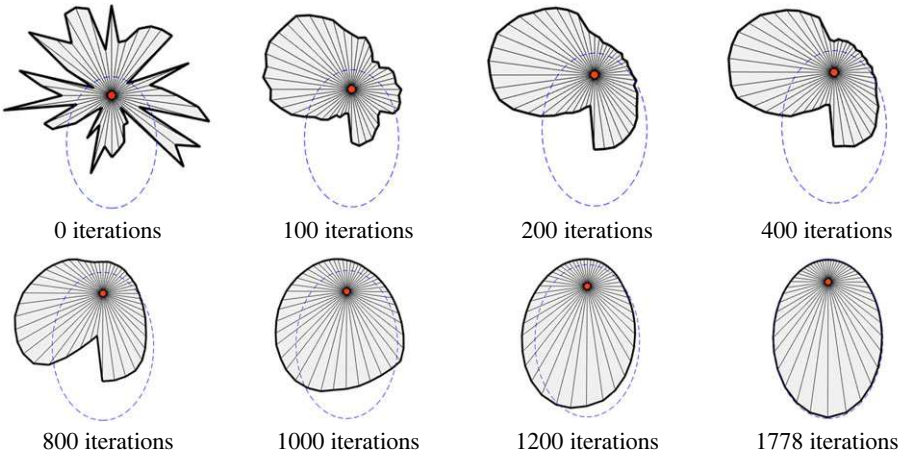


**Figure 9.** Evolution of the elliptical wheel shape during optimization. The design begins as an arbitrary polygon whose vertices are randomly distributed throughout the *xy*-plane. Through an iterative process, the design converges to the optimal wheel shape indicated by the dashed blue line.

wheel shape by moving the vertices of the polygon, which is used to approximate the elliptical wheel. Note that the vertices are initially scattered randomly in the *xy*-plane with the wheel shape obtained by connecting these points in a clockwise sequence.

## (b) Structural topology optimization

To obtain the internal structural design of the wheel and the barrow, we use a multi-layer topology optimization formulation. Here the internal structure of the wheel component and the barrow component are optimized simultaneously, with loads being transmitted from the barrow to the wheel via the axle. Figure 10 (rows 1–4) shows the evolution of the wheel and barrow components for both the circular (flat terrain) and the elliptical (sinusoidal terrain) wheel shapes. Note that in the topology optimization phase, all structures begin as a black box in which the entire design domain is populated with material. Within each iteration of the optimization procedure, the algorithm simulates the rolling motion of the current design by breaking the motion down into a series of rotational increments.

During the topology optimization, we assume a fixed wheel shape, which has been passed down from the shape optimization algorithm, and we optimize for a series of discrete load cases corresponding to different orientations assumed by the wheel during each rolling increment, with the ground serving as a fixed reference frame. The objective of the topology optimization problem is to minimize the mass of the wheelbarrow while ensuring that the system is sufficiently stiff with respect to all loading scenarios. Enforcing a lower bound on structural stiffness helps to mitigate inelastic deformations during rolling, thereby reducing energy dissipation due to hysteresis.

## (c) Combined shape and topology optimization

We also created a combined shape and topology optimization algorithm that allows us to simultaneously optimize the outer wheel shape along with the internal topologies of both the wheel and barrow components. This problem is particularly challenging because as the wheel's outer shape evolves, the location of the contact point for each orientation angle (i.e. load case) also changes from one iteration to the next. The contact model presented in §2(f) allows us to ensure that the function used to define the design objective remains smooth and continuous despite the changing contact point location. Figure 10 (rows 5 and 6) shows the evolution of the wheel and barrow components for the combined shape and topology optimization problem. Note that the red markers indicate the locations of the control points that form the outer shape of the wheel.

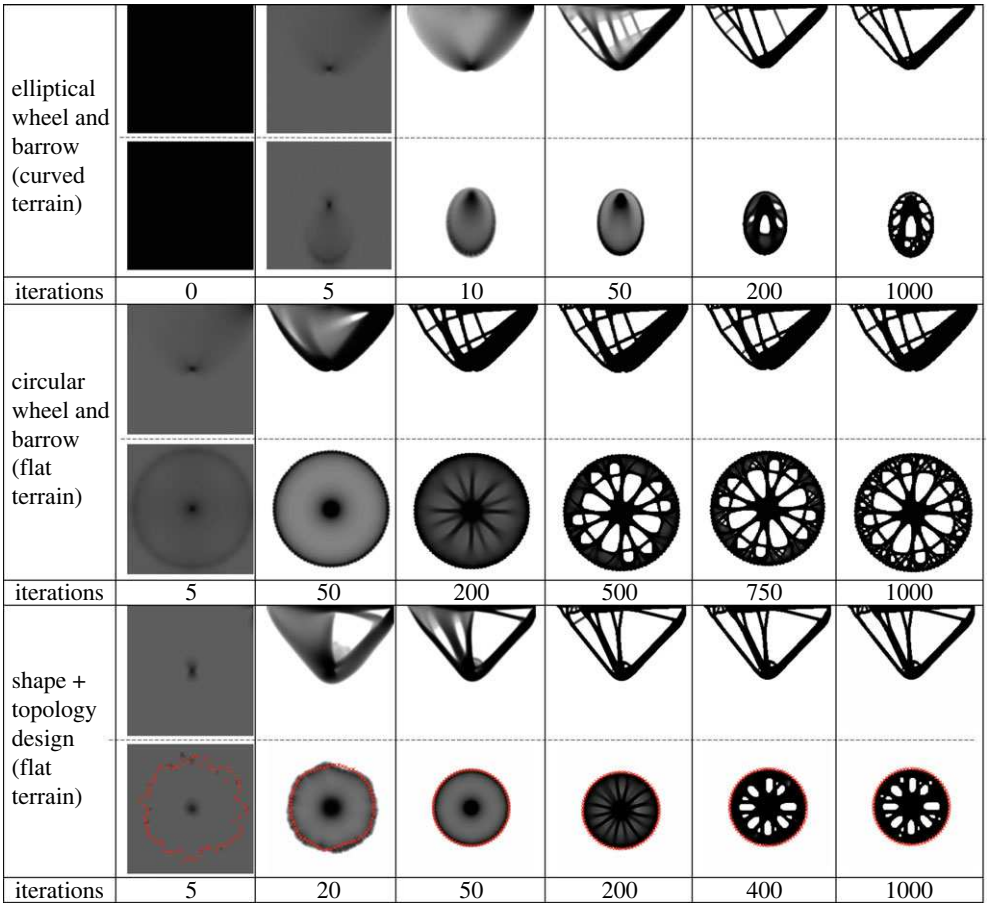


**Figure 10.** Evolution of the structural topology of the wheelbarrow system. For each the design, the barrow component is shown on the top row and the wheel component is shown below. The algorithm iteratively progresses toward an optimal structure by systematically removing material from the black box domain. Note that in the early stages of the algorithm, the black box is fully populated with material, hence the appearance of solid black and solid grey boxes in the far left column.

These points are initially distributed randomly throughout the design domain, and the optimizer prioritizes arranging these points into a circular formation before proceeding to optimize the wheel's internal structure.

From the material distributions shown in figure 10, we can extract the precise location of the material surface. We then extrude the resulting contour in the z-axis to obtain a three-dimensional interpretation of the computationally generated wheelbarrow designs. Figure 11 shows three-dimensional CAD (computer-aided design) renderings of all three wheelbarrow designs, along with a 3D printed prototype of the circular wheelbarrow.

## (d) Additional terrain profiles

To demonstrate the applicability of our algorithm to more complex terrains, we present two additional examples. The first is for a terrain in the shape of a triangle wave:

$$T(X) = \frac{2A_T}{\lambda_T}\left|\mathrm{mod}\left(\left(X - \frac{\lambda_T}{2}\right), \lambda_T\right) - \frac{\lambda_T}{2}\right|, \tag{3.1}$$

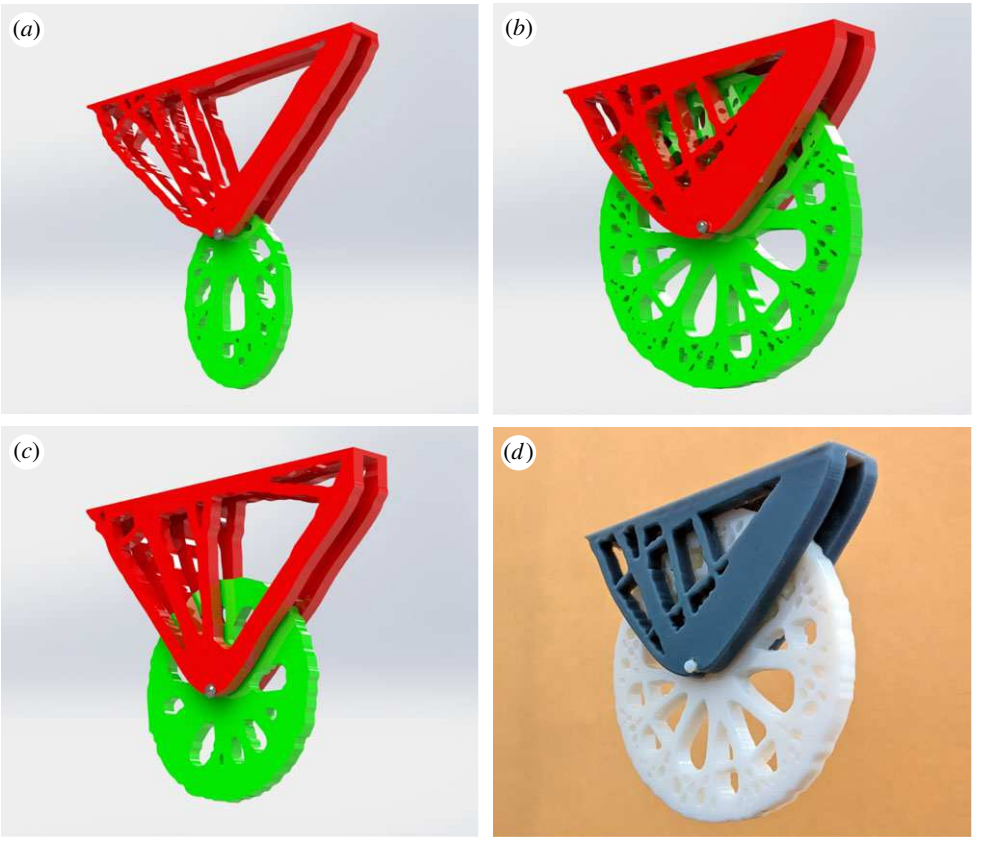


**Figure 11.** CAD renderings and 3D printed prototype of computationally designed wheelbarrow mechanisms. The 3D printed wheelbarrow is fully functional with the wheel able to rotate freely about the axle. (*a*) Elliptical wheelbarrow. (*b*) Circular wheelbarrow. (*c*) Shape and topology optimized wheelbarrow. (*d*) Three-dimensional printed circular wheelbarrow.

where, again, $A_T$ is the maximum elevation (i.e. amplitude), and $\lambda_T$ is the terrain's wavelength, as in equation (2.1). The second pattern is that of an elliptical wave defined by:

$$T(X) = \frac{b}{\sqrt{1 - ((a^2 - b^2)/a^2)\sin^2(\pi X/\lambda_T)}} - b, \tag{3.2}$$

where $a$ and $b$ are chosen constants. The optimal wheelbarrow topologies for each of these terrain shapes are shown in figure 12.

The optimal wheel shapes rolling over their respective terrains are depicted in figure 13. The images in figures 11–13 are notable in that they reveal a series of mechanisms whose function is unlike anything found in nature, yet their material patterns have a highly organic appearance, which distinguishes them from conventional wheeled vehicles. The ability of the algorithm to autonomously synthesize a system with this type of complexity represents a significant advancement in computational design and design automation.

## 4. Conclusion

In this study, we have introduced a novel method for automated computational synthesis of multi-body wheeled mechanisms. We implemented structural topology optimization to simultaneously generate the optimal geometry and material layout of the various components of the mechanism, which include a wheel and a carriage component. The topology optimization is coupled to a shape optimization scheme used to obtain the optimal wheel shape for a given

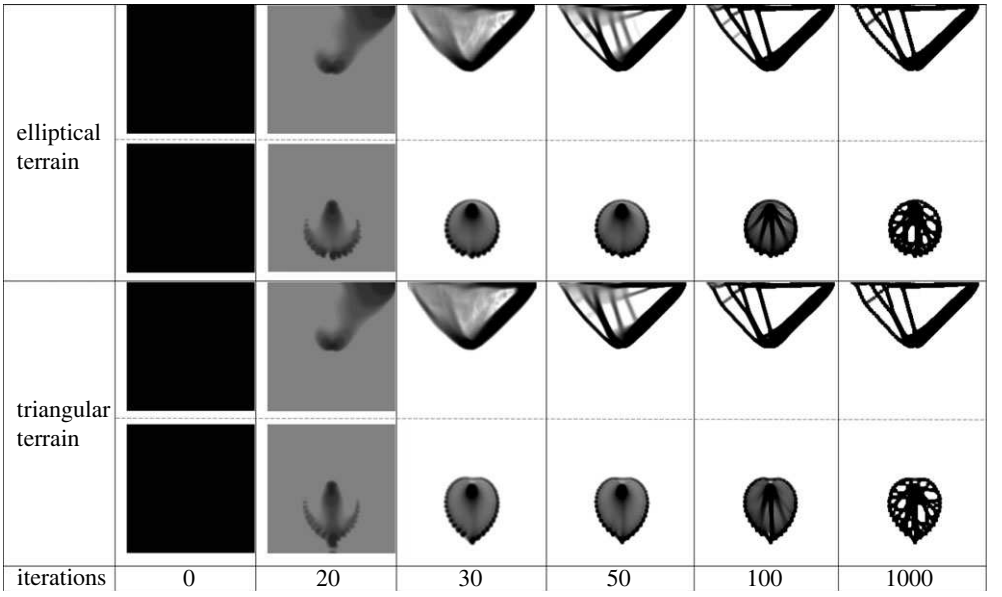


**Figure 12.** Evolution of the structural topology of the wheelbarrow systems designed for periodic terrain. The solution for the elliptical terrain is shown in the top two rows, and the triangular terrain in the bottom two rows.

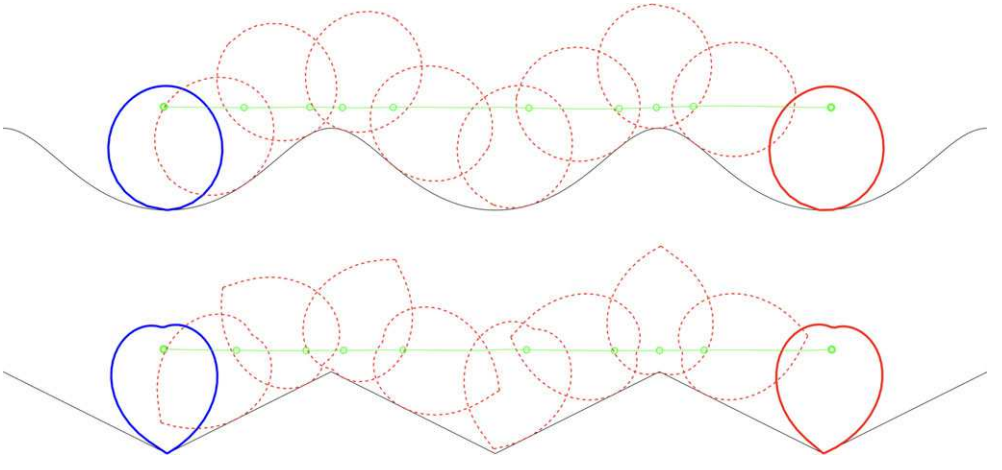

**Figure 13.** Optimal wheel shapes rolling over their elliptical and triangular terrains.

terrain profile. We also devised an original stiffness-based contact model that simulated the interaction between the wheel circumference and the ground. We demonstrated the method using examples containing flat, level terrain as well as several topographically periodic terrains. In each example, the algorithm converged to a feasible design whose wheel shape was consistent with analytical solutions, and whose structural topology satisfied the imposed stiffness constraints. This study demonstrates how gradient-based methods can be used to generate designs for complex mechanical systems while starting from a *black box*. Additionally, the results show that gradient-based methods can succeed even in contexts where the physics of the system being designed contains nonlinear and discontinuous phenomena such as variable surface contact. Future investigation will seek to expand the method to synthesize similarly complex and

foundational mechanical systems containing multiple rotating components, such as pulleys and gearboxes.

Data accessibility. All metadata and computer code used to generate the results presented in this study are publicly available from the Zenodo repository: https://zenodo.org/badge/latestdoi/408586352 [58].

Declaration of AI use. We have not used AI-assisted technologies in creating this article.

Authors' contributions. K.A.J.: conceptualization, data curation, formal analysis, funding acquisition, investigation, methodology, project administration, resources, software, supervision, validation, visualization, writing—original draft, writing—review and editing; P.L.K.: conceptualization, data curation, formal analysis, investigation, methodology, software, validation, visualization, writing—original draft, writing—review and editing; Z.K.: conceptualization, formal analysis, investigation, methodology, software, validation, visualization, writing—review and editing; A.B.: data curation, formal analysis, software, validation, visualization, writing—review and editing; L.R.A.: conceptualization, data curation, formal analysis, investigation, methodology, software, writing—review and editing.

All authors gave final approval for publication and agreed to be held accountable for the work performed therein.

Conflict of interest declaration. The authors declare that they have no competing interests.

Funding. This work was funded by the National Science Foundation (grant no. 1752054).

## References

1. Christensen PW, Klarbring A. 2008 *An introduction to structural optimization*, vol. 153. Berlin, Germany: Springer Science & Business Media.
2. Baandrup M, Sigmund O, Polk H, Aage N. 2020 Closing the gap towards super-long suspension bridges using computational morphogenesis. *Nat. Commun.* **11**, 1–7. (doi:10.1038/s41467-020-16599-6)
3. Wang Z, Tamijani AY. 2022 Computational synthesis of large-scale three-dimensional heterogeneous lattice structures. *Aerosp. Sci. Technol.* **120**, 107258. (doi:10.1016/j.ast.2021.107258)
4. Kumar P, Schmidleithner C, Larsen NB, Sigmund O. 2021 Topology optimization and 3D printing of large deformation compliant mechanisms for straining biological tissues. *Struct. Multidiscip. Optim.* **63**, 1351–1366. (doi:10.1007/s00158-020-02764-4)
5. Alacoque L, James KA. 2022 Topology optimization with variable loads and supports using a super-Gaussian projection function. *Struct. Multidiscip. Optim* **65**, 50. (doi:10.1007/s00158-021-03128-2)
6. Clausen A, Wang F, Jensen JS, Sigmund O, Lewis JA. 2015 Topology optimized architectures with programmable Poisson's ratio over large deformations. *Adv. Mater.* **27**, 5523–5527. (doi:10.1002/adma.201502485)
7. Lipson H, Pollack JB. 2000 Automatic design and manufacture of robotic lifeforms. *Nature* **406**, 974–978. (doi:10.1038/35023115)
8. Starling AC, Shea K. 2005. In *International Design Engineering Technical Conferences and Computers and Information in Engineering Conference, Long Beach, CA, 24–28 September 2005*, vol. 4739, pp. 427–436. New York, NY: ASME.
9. Wijkniet J, Hofman T. 2018 Modified computational design synthesis using simulation-based evaluation and constraint consistency for vehicle powertrain systems. *IEEE Trans. Veh. Technol.* **67**, 8065–8076. (doi:10.1109/TVT.2018.2844024)
10. Bendsøe MP. 1989 Optimal shape design as a material distribution problem. *Struct. Optim.* **1**, 193–202. (doi:10.1007/BF01650949)
11. Bendsøe MP, Kikuchi N. 1988 Generating optimal topologies in structural design using a homogenization method. *Comput. Methods Appl. Mech. Eng.* **71**, 197–224. (doi:10.1016/0045-7825(88)90086-2)
12. Nakshatrala PB, Tortorelli DA. 2015 Topology optimization for effective energy propagation in rate-independent elastoplastic material systems. *Comput. Methods Appl. Mech. Eng.* **295**, 305–326. (doi:10.1016/j.cma.2015.05.004)
13. Fan W, Xu Z, Wu B, He Y, Zhang Z. 2022 Structural multi-objective topology optimization and application based on the criteria importance through intercriteria correlation method. *Eng. Optim.* **54**, 830–846. (doi:10.1080/0305215X.2021.1901087)

14. Park J, Sutradhar A, Shah JJ, Paulino GH. 2018 Design of complex bone internal structure using topology optimization with perimeter control. *Comput. Biol. Med.* **94**, 74–84. (doi:10.1016/j.compbiomed.2018.01.001)
15. Aage N, Andreassen E, Lazarov BS, Sigmund O. 2017 Giga-voxel computational morphogenesis for structural design. *Nature* **550**, 84–86. (doi:10.1038/nature23911)
16. Andersen LG, Larsen JK, Fraser ES, Schmidt B, Dyre JC. 2015 Rolling resistance measurement and model development. *J. Transp. Eng.* **141**, 4014075. (doi:10.1061/(ASCE)TE.1943-5436.0000673)
17. Maute K, Allen M. 2004 Conceptual design of aeroelastic structures by topology optimization. *Struct. Multidiscip. Optim.* **27**, 27–42. (doi:10.1007/s00158-003-0362-z)
18. James KA, Kennedy GJ, Martins JRRA. 2014 Concurrent aerostructural topology optimization of a wing box. *Comput. Struct.* **134**, 1–17. (doi:10.1016/j.compstruc.2013.12.007)
19. Jensen PDL, Wang F, Dimino I, Sigmund O. 2021 Morphing Wing Structures. *Actuators* **10**, 217.
20. James KA, Waisman H. 2016 Layout design of a bi-stable cardiovascular stent using topology optimization. *Comput. Methods Appl. Mech. Eng.* **305**, 869–890. (doi:10.1016/j.cma.2016.02.036)
21. Xue H, Luo Z, Brown T, Beier S. 2020 Design of self-expanding auxetic stents using topology optimization. *Front. Bioeng. Biotechnol.* **8**, 736. (doi:10.3389/fbioe.2020.00736)
22. Patel JH, Poojari R, Shah MK, Shah AH, Khatawate VH. 2020. Topology Optimization of Wheel Hub Used in Automobiles. In *Proc. of Int. Conf. on Intelligent Manufacturing and Automation*, *Mumbai, India, 27–28 March 2020*, pp. 723–736. Berlin, Germany: Springer.
23. Jang S, Kang N. 2020 Generative design by reinforcement learning: Maximizing diversity of topology optimized designs. (http://arxiv.org/abs/2008.07119)
24. Christiansen AN, Bærentzen JA, Nobel-Jørgensen M, Aage N, Sigmund O. 2015 Combined shape and topology optimization of 3D structures. *Comput. Graph.* **46**, 25–35. (doi:10.1016/j.cag.2014.09.021)
25. Takezawa A, Nishiwaki S, Kitamura M. 2010 Shape and topology optimization based on the phase field method and sensitivity analysis. *J. Comput. Phys.* **229**, 2697–2718. (doi:10.1016/j.jcp.2009.12.017)
26. Ansola R, Canales J, Tarrago JA, Rasmussen J. 2002 An integrated approach for shape and topology optimization of shell structures. *Comput. Struct.* **80**, 449–458. (doi:10.1016/S0045-7949(02)00019-6)
27. Hassani B, Tavakkoli SM, Ghasemnejad H. 2013 Simultaneous shape and topology optimization of shell structures. *Struct. Multidiscip. Optim.* **48**, 221–233. (doi:10.1007/s00158-013-0894-9)
28. Amir O, Shakour E. 2018 Simultaneous shape and topology optimization of prestressed concrete beams. *Struct. Multidiscip. Optim.* **57**, 1831–1843. (doi:10.1007/s00158-017-1855-5)
29. Manios SE, Lagaros ND, Nassiopoulos E. 2019 Nested topology optimization methodology for designing two-wheel chassis. *Front. Built Environ.* **5**, 34. (doi:10.3389/fbuil.2019.00034)
30. Leger PC, Bares J. 1999. Automated Task-Based Synthesis and Optimization of Field Robots. In *Proc. of 2nd Int. Conf. on Field and Service Robotics* (*FSR '99*), *Pittsburgh, PA, 29–31 August 1999*.
31. Ben Abdallah MA, Khemili I, Aifaoui N. 2016 Dynamic synthesis of a flexible multibody system. *Int. J. Mech. Mechatron. Eng.* **10**, 1810–1815.
32. Pappalardo CM, Manca AG, Guida D. 2021 A combined use of the multibody system approach and the finite element analysis for the structural redesign and the topology optimization of the latching component of an aircraft hatch door. *IAENG Int. J. Appl. Math.* **51**, 175–191.
33. Luo R, Wu P, Yu Z, Hou Z. 2023 An overlapped plane model and topology optimization for planar mechanism synthesis. *Comput. Struct.* **281**, 107019. (doi:10.1016/j.compstruc.2023.107019)
34. Kim SI, Kang SW, Yi Y, Park J, Kim YY. 2018 Topology optimization of vehicle rear suspension mechanisms. *Int. J. Numer. Methods Eng.* **113**, 1412–1433. (doi:10.1002/nme.5573)
35. Briot S, Goldsztejn A. 2018 Topology optimization of industrial robots: application to a five-bar mechanism. *Mech. Mach. Theory.* **120**, 30–56. (doi:10.1016/j.mechmachtheory.2017.09.011)
36. Nemec M, Zingg DW, Pulliam TH. 2004 Multipoint and multi-objective aerodynamic shape optimization. *AIAA J.* **42**, 1057–1065. (doi:10.2514/1.10415)
37. Svanberg K. 1987 The method of moving asymptotes—a new method for structural optimization. *Int. J. Numer. Methods Eng.* **24**, 359–373. (doi:10.1002/nme.1620240207)

38. Rozvany GIN, Zhou M, Birker T. 1992 Generalized shape optimization without homogenization. *Struct. Optim.* **4**, 250–252. (doi:10.1007/BF01742754)
39. James KA, Waisman H. 2014 Failure mitigation in optimal topology design using a coupled nonlinear continuum damage model. *Comput. Methods Appl. Mech. Eng.* **268**, 614–631. (doi:10.1016/j.cma.2013.10.022)
40. Allaire G, Jouve F, Toader A-M. 2004 Structural optimization using sensitivity analysis and a level-set method. *J. Comput. Phys.* **194**, 363–393. (doi:10.1016/j.jcp.2003.09.032)
41. Alonso C, Querin OM, Ansola R. 2013 A sequential element rejection and admission (SERA) method for compliant mechanisms design. *Struct. Multidiscip. Optim.* **47**, 795–807. (doi:10.1007/s00158-012-0862-9)
42. Wang SY, Tai K. 2005 Structural topology design optimization using genetic algorithms with a bit-array representation. *Comput. Methods Appl. Mech. Eng.* **194**, 3749–3770. (doi:10.1016/j.cma.2004.09.003)
43. Nie Z, Lin T, Jiang H, Kara LB. 2021 Topologygan: topology optimization using generative adversarial networks based on physical fields over the initial domain. *J. Mech. Des.* **143**, 031715. (doi:10.1115/1.4049533)
44. Norato JA, Bell BK, Tortorelli DA. 2015 A geometry projection method for continuum-based topology optimization with discrete elements. *Comput. Methods Appl. Mech. Eng.* **293**, 306–327. (doi:10.1016/j.cma.2015.05.005)
45. Wang SY, Lim KM, Khoo BC, Wang MY. 2007 On hole nucleation in topology optimization using the level set methods. *Comput. Model. Eng. Sci.* **21**, 219.
46. Sigmund O. 2011 On the usefulness of non-gradient approaches in topology optimization. *Struct. Multidiscip. Optim.* **43**, 589–596. (doi:10.1007/s00158-011-0638-7)
47. Sigmund O, Petersson J. 1998 Numerical instabilities in topology optimization: a survey on procedures dealing with checkerboards, mesh-dependencies and local minima. *Struct. Optim.* **16**, 68–75. (doi:10.1007/BF01214002)
48. Guest JK. 2009 Topology optimization with multiple phase projection. *Comput. Methods Appl. Mech. Eng.* **199**, 123–135. (doi:10.1016/j.cma.2009.09.023)
49. Bruns TE, Tortorelli DA. 2001 Topology optimization of non-linear elastic structures and compliant mechanisms. *Comput. Methods Appl. Mech. Eng.* **190**, 3443–3459. (doi:10.1016/S0045-7825(00)00278-4)
50. James KA, Hansen JS, Martins JRRA. 2009 Structural topology optimization for multiple load cases using a dynamic aggregation technique. *Eng. Optim.* **41**, 1103–1118. (doi:10.1080/03052150902926827)
51. Swartz KE, James KA. 2019 Gaussian layer connectivity parameterization: a new approach to topology optimization of multi-body mechanisms. *CAD Comput. Aided Des.* **115**, 42–51. (doi:10.1016/j.cad.2019.05.008)
52. Lawry M, Maute K. 2015 Level set topology optimization of problems with sliding contact interfaces. *Struct. Multidiscip. Optim.* **52**, 1107–1119. (doi:10.1007/s00158-015-1301-5)
53. Kristiansen H, Poulios K, Aage N. 2020 Topology optimization for compliance and contact pressure distribution in structural problems with friction. *Comput. Methods Appl. Mech. Eng.* **364**, 112915. (doi:10.1016/j.cma.2020.112915)
54. Aharoni L, Bachelet I, Carstensen JV. 2021 Topology optimization of rigid interlocking assemblies. *Comput. Struct.* **250**, 106521. (doi:10.1016/j.compstruc.2021.106521)
55. Bluhm GL, Sigmund O, Poulios K. 2021 Internal contact modeling for finite strain topology optimization. *Comput. Mech.* **67**, 1099–1114. (doi:10.1007/s00466-021-01974-x)
56. Ghandriz T, Führer C, Elmqvist H. 2017 Structural topology optimization of multibody systems. *Multibody. Syst. Dyn.* **39**, 135–148. (doi:10.1007/s11044-016-9542-7)
57. Cherkaev A. 2000 *Variational methods for structural optimization*, vol. 140. Berlin, Germany: Springer Science & Business Media. See http://www.math.utah.edu/books/vmso/.
58. Kai J. 2022. Code for: kaijames1/wheeldesign: (v3.0). *Zenodo*. (doi:10.5281/zenodo.6321472)